High-Power Cooperative Jamming with Nonlinear Known-Interference Cancellation

KAREL PÄRLIN
MATIAS TURUNEN
Tampere University, Tampere, Finland

AARON BYMAN, Member, IEEE
TOMMI MERILÄINEN
Bittium, Oulu, Finland

VINCENT LE NIR
Royal Military Academy, Brussels, Belgium

MARC ADRAT
Fraunhofer FKIE, Wachtberg, Germany

TANELI RIIHONEN, Senior Member, IEEE
Tampere University, Tampere, Finland

Abstract—This article proposes a nonlinear known-interference cancellation (KIC) algorithm that allows a receiver to suppress the interference from a high-power cooperative jammer given that the transmitted interference is known in advance to the receiver. The proposed algorithm achieves this by estimating and compensating for the nonlinear power amplifier (PA) distortions, wireless channel effects, and frequency offsets that alter the transmitted interference as it propagates to the receiver. Measurements with commercial off-the-shelf radio platforms in both laboratory and outdoor conditions are presented. Their results demonstrate that the proposed method is able to cancel known interference (KI) with moderate residuals for a wide range of received signal-to-interference-plus-noise ratios (SINRs). This facilitates processing a signal of interest that is otherwise masked by the interference signal.
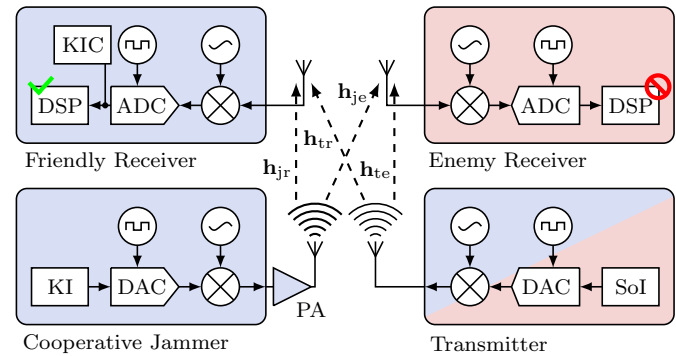
Fig. 1. System model — cooperative jamming prevents unauthorized nodes, but not authorized nodes with KIC, from accessing the EMS.

Index Terms— Communication system security, electronic countermeasures, electronic jamming, electronic masking, interference suppression, nonlinear distortions, physical layer security.

I. INTRODUCTION

MODERN battlefields depend on the electromagnetic spectrum (EMS) for many operational capabilities, such as communication, intelligence collection, and navigation. Through serving as a resource for these capabilities, EMS is a local operational environment that connects together all of the warfighting domains (land, sea, air, space, and cyber) that use it. This necessitates careful cross-domain EMS management so that cooperating forces do not unintentionally interfere with each other. Furthermore, EMS is often targeted between opposing forces through electronic warfare because gaining an advantage over an adversary in the EMS is also helpful to advancing military objectives [1]. Jamming, e.g., is oftentimes used to prevent enemy units from communicating or using radars [2]. Such electronic attacks need to be especially carefully managed so as not to overlap in time and frequency with other operations in the EMS and not cause interference to the cooperative forces.

If different operations in the EMS could be carried out simultaneously on the same frequency without interfering with each other, then this would improve not only EMS usage efficiency but also reliability and security [3], [4]. Combining simultaneous same-frequency transmit and receive operations in a single radio is already becoming feasible with full-duplex (FD) radio technology by using self-interference cancellation (SIC) to suppress the interference that the transmit front-end of a radio inevitably causes to its own receive front-end [5]. This allows to, e.g., simultaneously receive a communication signal while also transmitting a jamming signal to prevent eavesdropping [6]. Success of such operation relies on sufficient SIC [7] but even with that achieved, the benefits of multifunction FD operation are often limited to a single FD-capable radio [8]. In order to extend these benefits to multiple radios as envisioned in Fig. 1, the capability to cancel KI across separate radios is necessary.

Canceling the KI received from another radio is, however, more challenging than canceling self-interference because of the inevitable carrier and sampling frequency offsets between any two radios. For KIC to be practical, the channel from the KI transmitter to receiver needs to be estimated and compensated for together with these offsets [9]–[16]. Few linear KIC methods have already been proposed by others for estimating the wireless channel under a carrier frequency offset and with varying level of attention to the sampling frequency offset but without modeling PA nonlinearities in [17]–[19]. Moreover, the methods in [17], [19] rely on the KI being repetitive for the parameter estimation, which can benefit the adversary, and the approach in [18] combines the parameters in an implicit manner, which prevents decoupling the estimates. A nonlinear KIC method for estimating the wireless channel and PA nonlinearities under a carrier frequency offset through memory polynomial kernels has been proposed in [20], [21] and extended to include time alignment in [22]. The method in [22] is intriguing but again combines all parameters implicitly and relies on one of the computationally less efficient methods for estimating and modeling nonlinear distortions [23]. All these methods have been verified either by simulations or by experiments in laboratories but results from practical (outdoor) conditions have not yet been reported.

In this work, we propose a nonlinear KIC method that estimates the transmitter PA nonlinearities, wireless propagation paths, plus carrier and sampling frequency offsets, relying only on the transmitted KI being known but not on being of any certain structure. The proposed method estimates and tracks the above-listed effects separately from one-another, which allows a reduction in the number of required computations when some parameter updates can be put on hold (e.g., slow time-varying PA distortions) or parameters can be stored (e.g., in frequency hopping). The proposed nonlinear KIC method builds on our linear KIC method [24], [25] that we have previously extended to suppress KI from multiple cooperative jammers simultaneously [26] and to suppress wideband KI when only a narrowband portion of it has been received [27]. Nonlinear distortion modeling in this work is added through spline-based interpolation that performs comparably to memory polynomial-based models but with substantially lower complexity [23], [28]. Finally, we study the performance of the proposed nonlinear KIC method in both laboratory and outdoor environments and, based on the measurements results, analyze how high-power cooperative jamming together with KIC affects EMS access across a geographical area.

The rest of this article is organized as follows. The system model and the proposed nonlinear KIC algorithm are introduced in Section II. The setups of and results from laboratory and outdoor measurements are presented in Section III and Section IV, respectively. The measurement results are used to model performance over a certain area in Section V. And, finally, the article is concluded in Section VI.

Notation: In this article, small boldface letters are used to denote vectors and capital boldface letters to denote matrices, e.g., $\mathbf{h} \in \mathbb{C}^{M \times 1} = [h_1 \ h_2 \ \cdots \ h_M]^T$ and $\mathbf{A} \in \mathbb{C}^{M \times N}$. By default, vectors are column vectors. The iteration index is placed as a subscript for vectors and between parentheses for scalars, e.g., $\mathbf{h}_n$ and $v(n)$. Transpose, Hermitian transpose, and complex conjugate are denoted by $(\cdot)^T$, $(\cdot)^H$, and $(\cdot)^*$, respectively. Absolute value is denoted by $|\cdot|$ and floor operator by $\lfloor \cdot \rfloor$. And lastly, the real and imaginary operators are denoted by $\Re\{\cdot\}$ and $\Im\{\cdot\}$, respectively.

II. NONLINEAR KNOWN-INTERFERENCE CANCELLATION

A. System Model

The system model in this work follows that in Fig. 1. The transmitter broadcasts a signal $s(t)$, the contents of which are unknown but of interest to both receivers. Simultaneously, the cooperative jammer broadcasts a signal $G^o(x(t))$, where $G^o(\cdot)$ denotes the nonlinear gain of the PA and $x(t)$ is the KI that, in its discrete-time baseband complex form $x(n)$, is known only to the friendly receiver. Then, the discrete-time signal at the friendly receiver is a superposition of the two signals as

$$d_{\mathrm{r}}(n) = \mathbf{h}_{\mathrm{jr}}^H G^o(\mathbf{y}_n^o) e^{j\phi^o(n)} + \mathbf{h}_{\mathrm{tr}}^H \mathbf{s}_n + v_{\mathrm{r}}(n), \quad (1)$$

where $\mathbf{h}_{\mathrm{jr}}$ and $\mathbf{h}_{\mathrm{tr}}$ are the channel impulse responses from cooperative jammer and transmitter to the receiver respectively, $v_{\mathrm{r}}(n)$ represents measurement noise with variance σ_{v}^2, $\mathbf{y}_n^o$ accounts for sampling $x(t)$ with time-varying sampling frequency offset $\eta^o(i)$ according to (2) in [24] and includes the sampling jitter, and the multiplicative term $e^{j\phi^o(n)} = e^{j \sum_{i=1}^n \epsilon^o(i)}$ accounts for the carrier frequency offset and phase noise. The discrete-time signal at the enemy receiver becomes

$$d_{\mathrm{e}}(n) = \mathbf{h}_{\mathrm{je}}^H G^o(\mathbf{x}_n) + \mathbf{h}_{\mathrm{te}}^H \mathbf{s}_n + v_{\mathrm{e}}(n), \quad (2)$$

where $\mathbf{h}_{\mathrm{je}}$ and $\mathbf{h}_{\mathrm{te}}$ are the channel impulse responses from cooperative jammer and transmitter to the enemy receiver respectively, $v_{\mathrm{e}}(n)$ is the measurement noise with, again, variance σ_v, and the frequency offsets that affect $x(t)$ can be ignored, since the jamming signal is assumed to be unknown to the enemy receiver anyway.

The enemy receiver is left with the superposition of the two received signals. The friendly receiver, however, can subtract $x(n)$ from the received signal if it is able to estimate $\mathbf{h}_{\mathrm{jr}}$, $G^o(\cdot)$, $\epsilon^o(n)$, and $\eta^o(n)$, resulting in

$$e(n) = d_{\mathrm{r}}(n) - \mathbf{h}_n^H G_n(\mathbf{y}_n) e^{j\phi(n)}, \quad (3)$$

where $\mathbf{h}_n$, $G_n(\cdot)$, $\epsilon(n)$, and $\eta(n)$ are respectively the estimates of the channel impulse response, nonlinear gain, carrier frequency offset, and sampling frequency offset at iteration n, $\mathbf{y}_n$ is the result of resampling $x(n)$ with $\eta(n)$ according to (2) in [24], and $e^{j\phi(n)} = e^{j \sum_{i=1}^n \epsilon(i)}$. With precise parameter estimates, the error in (3) approximates to $e(n) \approx \mathbf{h}_{\mathrm{tr}}^H \mathbf{s}_n + v_{\mathrm{r}}(n)$, containing only the signal of interest and natural additive noise.

Based on the above, the SINRs with and without KIC can be written as

$$\gamma_{\mathrm{r}} = \frac{\frac{1}{N}\sum_{n=1}^{N}|\mathbf{h}_{\mathrm{tr}}^{H}\mathbf{s}_n|^2}{\frac{1}{N}\sum_{n=1}^{N}|e(n) - \mathbf{h}_{\mathrm{tr}}^{H}\mathbf{s}_n|^2} \tag{4}$$

and

$$\gamma_{\mathrm{e}} = \frac{\frac{1}{N}\sum_{n=1}^{N}|\mathbf{h}_{\mathrm{te}}^{H}\mathbf{s}_n|^2}{\frac{1}{N}\sum_{n=1}^{N}|\mathbf{h}_{\mathrm{je}}^{H}G^o(\mathbf{x}_n)|^2 + \sigma_{\mathrm{v}}^2}, \tag{5}$$

where N is the total number of $x(n)$ samples received. With precise parameter estimates, the SINR at the receiver approximates to that of the received signal without KI whereas the SINR at the eavesdropper is degraded by the received KI. In practice, close-but-imperfect parameter estimates will likely result in some residual KI at the receiver, degrading the SINR to a small extent there, too.

B. S-FO-LMS Algorithm

To estimate the system parameters, a gradient descent-based algorithm, the spline-interpolated and frequency offsets-compensated least mean squares (S-FO-LMS) filter, is here developed. S-FO-LMS updates the parameter estimates iteratively so that a nonnegative cost function is reduced with every iteration, generally ensuring convergence over time. In this work, we use as cost function the instantaneous square error

$$J(n) = |e(n)|^2 = e(n)e^*(n) \tag{6}$$

and derive update equations for each of the parameter estimates by taking partial derivatives of the cost function with respect to the parameters one by one. This results in a gradient vector that leads to update equations for minimizing the cost function. We have previously applied similar method for estimating the wireless channel under carrier and sampling frequency offsets but without the nonlinear distortions [24]–[27]. The nonlinear gain function $G_n(\cdot)$ does not lend itself conveniently for adaptation. However, nonlinear distortions can be efficiently modeled using spline-based approximation and the control points of splines themselves can be adapted using the gradient descent method [29].

Using spline-based interpolation, the nonlinear PA output $G_n(y(n))$ can be written as

$$G_n(y(n)) = y(n)(1 + \mathbf{\Psi}_n^T\mathbf{q}_n), \tag{7}$$

where $\mathbf{\Psi}_n$ and $\mathbf{q}_n$ are the spline basis functions and control points defined in Appendix A. Replacing the nonlinear gain function $G_n(\cdot)$ in (3) with that above, the error signal in (3) becomes

$$e(n) = d_{\mathrm{r}}(n) - \mathbf{h}_n^H\mathbf{r}_ne^{j\phi(n)}, \tag{8}$$

where

$$\mathbf{r}_n = [y(n)(1 + \mathbf{\Psi}_n^T\mathbf{q}_n)\ \ y(n-1)(1 + \mathbf{\Psi}_{n-1}^T\mathbf{q}_{n-1})$$
$$\cdots\ y(n-M+1)(1 + \mathbf{\Psi}_{n-M+1}^T\mathbf{q}_{n-M+1})]^T. \tag{9}$$

As such, the spline control points $\mathbf{q}_n$ model the PA nonlinearities, and the nonlinearities can be estimated and tracked through adapting the control points vector.
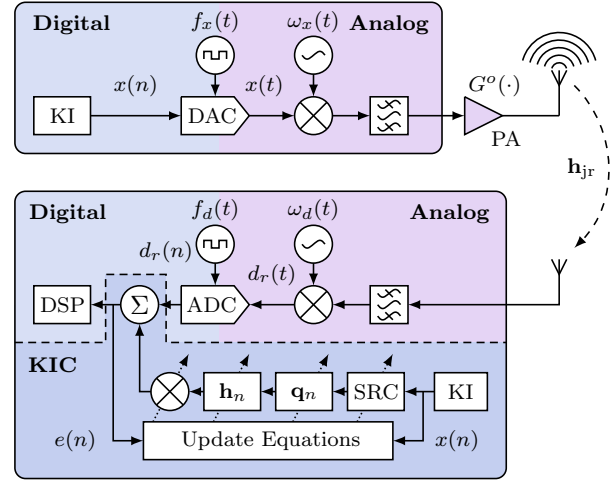

Fig. 2. Block diagram of the proposed nonlinear KIC method.

The update rules for $\mathbf{h}_n$, $\mathbf{q}_n$, $\epsilon(n)$, and $\eta(n)$ are derived in full in Appendix B but the final update equations are

$$\mathbf{h}_{n+1} = \mathbf{h}_n + \mu_{\mathrm{h}}e^*(n)\mathbf{r}_ne^{j\phi(n)}, \tag{10a}$$

$$\mathbf{q}_{n+1} = \mathbf{q}_n + \mu_{\mathrm{q}}e(n)\mathbf{\Sigma}_n^T\mathbf{Y}_n^*\mathbf{h}_ne^{-j\phi(n)}, \tag{10b}$$

$$\epsilon(n+1) = \epsilon(n) - \mu_{\epsilon}\Im\{e^*(n)\mathbf{h}_n^H\mathbf{r}_ne^{j\phi(n)}\}, \tag{10c}$$

$$\eta(n+1) = \eta(n) + \mu_{\eta}\Re\{e^*(n)(\mathbf{h}_n^H\mathbf{r}_n)'e^{j\phi(n)}\}, \tag{10d}$$

where μ_{h}, μ_{q}, μ_{ϵ}, and μ_{η} are the adaptation step sizes, $\mathbf{Y}_n = \mathrm{diag}\{y(n), y(n-1), \cdots, y(n-M+1)\}$ contains the signal regression of $y(n)$ in its main diagonal, $\mathbf{\Sigma}_n = [\mathbf{\Psi}_n\ \mathbf{\Psi}_{n-1}\ \cdots\ \mathbf{\Psi}_{n-M+1}]^T$ contains the delayed M samples of $\mathbf{\Psi}_n$. The resulting KIC algorithm can be implemented before any digital signal processing stage as illustrated in Fig. 2 and in the open-source implementation provided with this work.[1] Computational complexity of the proposed algorithm in terms of required real-valued multiplications is summarized in Table I, assuming that Lagrange interpolation [30] with order L is used for the sample rate conversion. In addition to the multiplications, at each iteration a square root operation and $2L^2 - 2L$ real-valued divisions are needed.

---

[1]Link to the repository will be included here upon paper's publication.

TABLE I

Number of required arithmetic operations in each iteration.

| Computation		Real-valued multiplications
Cancellation	$y(n)$	$7L^2 - 7L$
	$r(n)$	$P^2 + 3P + 7$
	$e(n)$	$3M + 3$
Update equations	$\mathbf{h}_{n+1}$	$3M + 5$
	$\mathbf{q}_{n+1}$	$3Q + 3M + 8$
	$\epsilon(n+1)$	4
	$\eta(n+1)$	4
Total		$P^2 + 3P + 9M + 3Q$ $+7L^2 - 7L + 31$

III. LABORATORY MEASUREMENTS
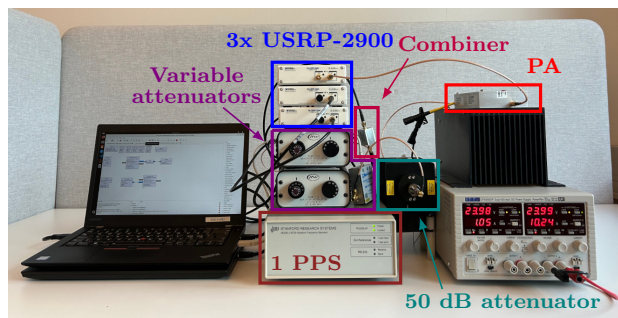
A. Measurement Setup

The laboratory measurements in this work were carried out using the setup illustrated in Fig. 3. This setup is a simplification of the system model in Fig. 1 as the setup includes only a single receiver, not two. This simplification reduced the amount of data that was recorded but does not limit the applicability of the measurements to the system model as the single used receiver can be considered friendly or adversarial in processing of the measurement data. All three measurement nodes were implemented using USRP-2900 software-defined radios that operated on the $302\,\mathrm{MHz}$ center frequency and used a digital intermediate frequency to reduce the impact of local oscillator leakages and IQ imbalances. During the laboratory measurements, the three nodes were connected over cables and an RF combiner, plus fixed and variable attenuators to control the SINR at the receiver.

The KI transmitted by the cooperative jammer was a $200\,\mathrm{kHz}$ band-limited noise signal, the samples of which were first drawn from a pseudo-random number generator with normal distribution, clipped for peak-to-average power ratio reduction, and then digitally filtered. This approach could be straightforwardly replicated in practical applications for generating the same KI waveform in multiple authorized nodes, relying only on a shared secret seed for the pseudo-random number generator. While in practice the KI waveform would preferably be of infinite length, the KI in these measurements repeated so that the exact same KI waveform could be used for cancellation over the large amount of recordings produced. Furthermore, the KI included a short repetitive sequence at its beginning so that the receiver could, through autocorrelation, achieve coarse synchronization for the received KI without any other coordination between the cooperative jammer and receiver. The KI was externally amplified using a Mini-Circuits ZHL-100W-52-S+ high-power amplifier and, unless noted otherwise, the PA was operated at its $1\,\mathrm{dB}$ compression point with peak output power of $48.5\,\mathrm{dBm}$.

The signal of interest broadcast by the transmitter was a $25\,\mathrm{kHz}$ continuous phase modulated NATO narrowband waveform (NBWF) in mode N1 [31], [32] with 70 frames at $30\,\mathrm{ksps}$ per recording. The transmitter and receiver were connected to a reference timing generator, which simplified processing the recordings since the position of the NBWF in the received signal is precisely known. This merely reduced the amount of processing time that the NBWF demodulator required in looking for the waveform preambles. The two signals, KI and NBWF, were recorded superposed at the receiver with different SINRs and the recordings were processed offline using both linear and nonlinear KIC with memory length $M = 5$, number of spline control points $Q = 19$, and step sizes that were empirically deemed to provide good steady-state performance. In cases where "perfect KIC" is referred to, the recording was actually done without any KI.
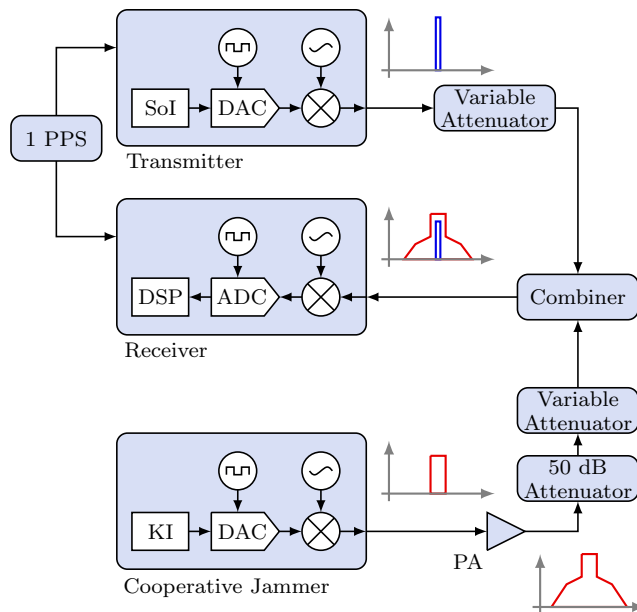
(a) Diagram of the setup

(b) Photo of the setup

Fig. 3. Laboratory measurement setup.

B. Measurement Results

An example of the two waveforms as recorded in the laboratory is given in Fig. 4. When the received KI is considerably more powerful than the received NBWF, as in the measurement illustrated in Fig. 4, then the NBWF signal will be masked by the KI and processing the NBWF is prevented. The figure also illustrates that the linear KIC is able to cancel the received KI down to the level of the nonlinear distortions in the received KI, as is expected [24], [25]. However, in this specific measurement the NBWF is then still masked by those nonlinear distortions. Only after applying nonlinear KIC is the NBWF signal unmasked. Although it is visible that the nonlinear KIC does not achieve perfect cancellation either. In general, this is due to the various modeling inaccuracies and time variations in the system. But the canceler's performance is also not helped by the received NBWF that from a certain SINR will act as interference to the KIC. The implications of this mutual interference become clearer by the end of this subsection.

Canceling a received KI signal is only really necessary when that KI superposes a signal of interest that is to be unmasked. However, analyzing KIC performance when
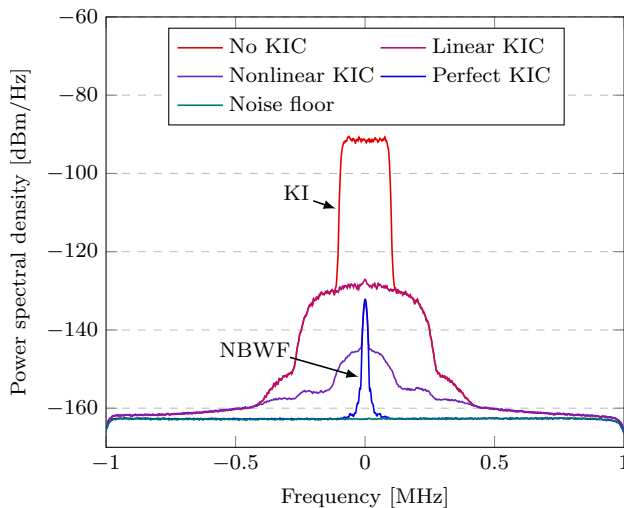
Fig. 4. Power spectral densities of the received superposed KI and NBWF in the laboratory measurements without KIC as well as with different variations of KIC.

Fig. 5. Linear and nonlinear KIC results in the laboratory environment with the cooperative jammer PA operated in three different states: at its $3\,\mathrm{dB}$ compression point, at its $1\,\mathrm{dB}$ compression point, and in its linear gain range (i.e., $0\,\mathrm{dB}$ compression).

there is no signal of interest provides insight into how well the KIC can be expected to work at its best. To that end, Fig. 5 shows how the linear and nonlinear KIC algorithms perform when only the KI is received. For the purpose of this specific analysis, and in order to examine how the two KIC algorithms perform when faced with different levels of nonlinear distortions, the cooperative jammer's PA was operated in three different states: at its $3\,\mathrm{dB}$ compression point, at its $1\,\mathrm{dB}$ compression point, and in its linear gain region.

The results show that the linear KIC achieves $33\,\mathrm{dB}$, $39\,\mathrm{dB}$, or $51\,\mathrm{dB}$ of cancellation while the nonlinear KIC achieves $56\,\mathrm{dB}$, $61\,\mathrm{dB}$, or $65\,\mathrm{dB}$ of cancellation, depending on which state the PA is operated at. This means that compensating for the nonlinear distortions provides up to $23\,\mathrm{dB}$ of additional cancellation when the PA is operated in its highly nonlinear region. Still, it is again evident that not even this improvement is enough to achieve perfect cancellation. Even though both algorithms track the carrier and sampling frequency offsets, the algorithms' performance is to some extent always limited by the rapid variations (i.e., phase noise and sampling jitter) in these offsets. In practical measurements, these variations can be expected to be compounded by those of the wireless channel. Finally, despite this is not illustrated in Fig. 5, measurement analysis showed that the two algorithms reached the levels presented in Fig. 5 with very similar convergence times of occasionally up to $20\,\mathrm{ms}$ but generally below $5\,\mathrm{ms}$.

Performance of the KI cancelers when the NBWF signal is received too is illustrated in terms of the demodulated NBWF's bit error rate (BER) in Fig. 6. The received KI power was kept fixed at $-45\,\mathrm{dBm}$ and the received NBWF power was varied in a $90\,\mathrm{dB}$ range with $2\,\mathrm{dB}$ steps, which resulted in the interference-to-signal ratios (ISRs) plotted on the x-axis. The upper layers of NBWF require the physical layer BER to remain below 10^{-4}
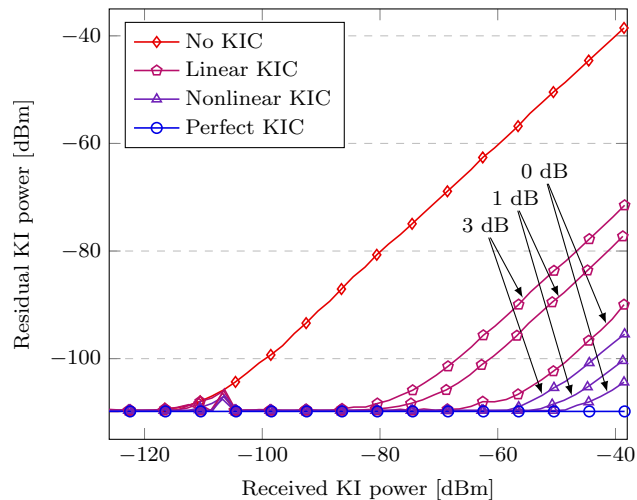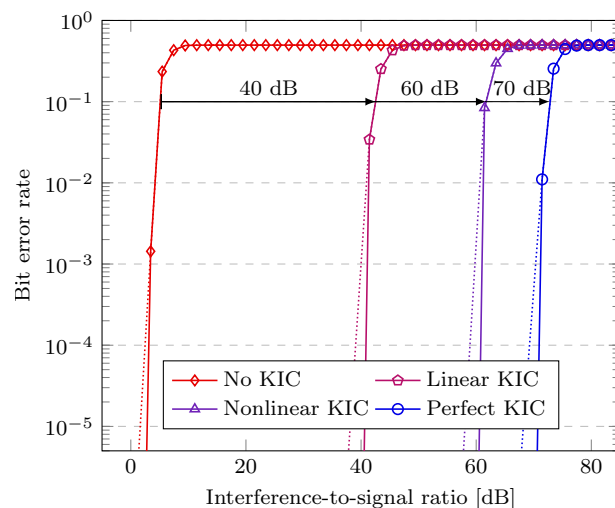

Fig. 6. NBWF demodulation performance under cooperative jamming without and with KIC. Measured and extrapolated results are plotted in solid and dotted lines, respectively.

for the communication link to function. However, the amount of NBWF data transmitted in the measurements together with attenuation steps limit the precision with what the BER can be calculated and the lowest non-zero BER that is reported. Importantly, in all cases the BER does reach zero, but for comparison of the KIC methods, the reliably measurable 10% BER is used here while the extrapolated results for BER at 10^{-4} will be used in Section V to provide functional communication areas. The results in Fig. 6 show that the cooperative jammer requires only some decibels of positive ISR to cause the received bits to be mostly erroneous when the receiver does not perform KIC. With linear and nonlinear KIC, the demodulator's performance improves by $40\,\mathrm{dB}$ and $60\,\mathrm{dB}$, respectively. These results demonstrate that the cancellation performance illustrated in Fig. 5 rather directly translates to improved NBWF processing.

Finally, Fig. 7 presents the estimated SINR without KIC (top), with linear KIC (middle), and with nonlinear KIC (bottom) when both the received NBWF and KI powers were varied in a $90\,\text{dB}$ range with $5\,\text{dB}$ steps. These results characterize the KICs' performance over a wide range of received SINRs that would likely occur in practical deployments. With perfect KIC, the SINR contour lines would be vertical, indicating indifference to the received KI power. Without KIC, the SINR is degraded in much of the grid. Fortunately, both linear and nonlinear KICs improve the SINR in large parts of those otherwise degraded areas. The nonlinear KIC especially improves the SINR at high received KI powers. Still, it must also be conceded here that the KICs are not always able to suppress the KI perfectly, causing some SINR degradation compared to perfect expectations.

IV. OUTDOOR MEASUREMENTS

A. Measurement Setup

The outdoor measurement setup is illustrated in Fig. 8 and it followed closely that of the laboratory measurements to facilitate direct comparison. For outdoor measurements the cables connecting the three devices were replaced by antennas and the attenuators after the cooperative jammer PA were removed. The cooperative jammer was fitted with a directive Yagi–Uda type FD antenna designed specifically for the $300\,\text{MHz}$ band [33] and the jammer was positioned facing east at the roof of a nine-story building (Kampusareena) at the Hervanta campus of Tampere University. The NBWF transmitter and receiver were both equipped with commercial off-the-shelf quarter wavelength monopole antennas that were attached to the roof of a motorized vehicle. This allowed to vary the received KI and NBWF powers by driving the vehicle and varying the attenuator at the transmitter, respectively, and ensured that received KI or NBWF power could be straightforwardly changed independently.

As a minor exception compared to the indoor measurements, outdoors the receiver was fitted with a Mini-Circuits ZX75BP-253-S+ passband filter (passband from 186 to $340\,\text{MHz}$) to avoid out-of-band interferences from saturating the receiver front-end. The vehicle was driven from where the received KI was close to saturating the receiver to where the received KI was below the receiver noise floor. Recordings were made with the van stopped at the side of the road at different points in that range. At each stopping point, the received KI was recorded without and with the NBWF. For recordings with the latter included, the NBWF transmit power was varied so that its received signal level would be $0\,\text{dB}$, $3\,\text{dB}$, $6\,\text{dB}$, $10\,\text{dB}$, $20\,\text{dB}$, $30\,\text{dB}$, and $40\,\text{dB}$ above the sensitivity level without KI. Finally, the memory length of the KIC algorithms was extended to $M = 41$ in order to accommodate multipath propagation and imprecision in the coarse synchronization.
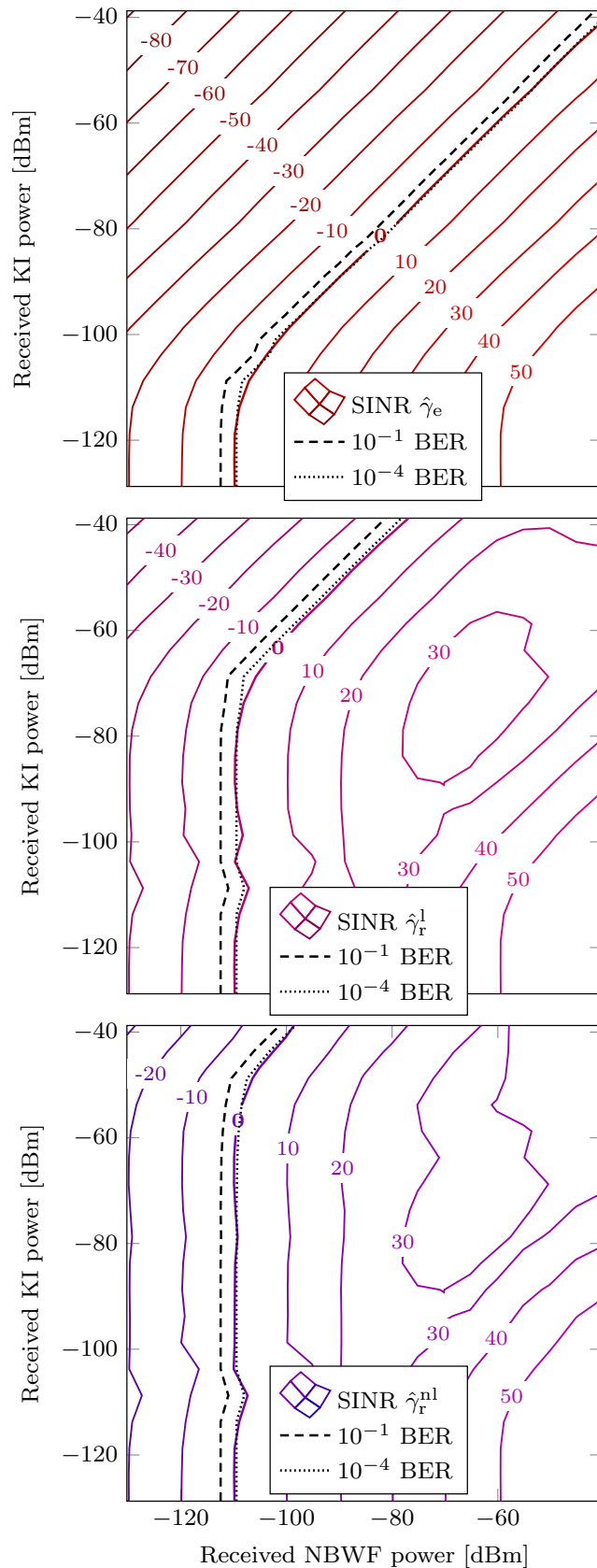

Fig. 7. Estimated SINRs without KIC ($\hat{\gamma}_{\text{e}}$), with linear KIC ($\hat{\gamma}_{\text{r}}^{\text{l}}$), and with nonlinear KIC ($\hat{\gamma}_{\text{r}}^{\text{nl}}$) including the measured 10% and extrapolated 10^{-4} BER thresholds with regards to the received NBWF and KI signal levels.
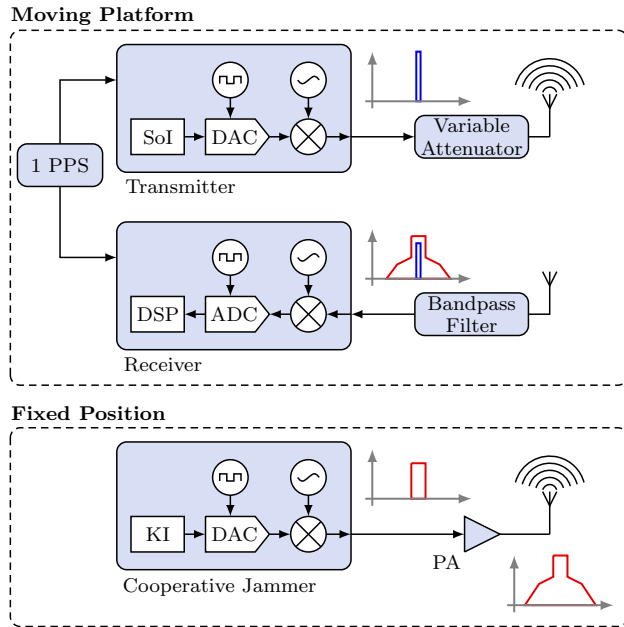
(a) Diagram of the setup
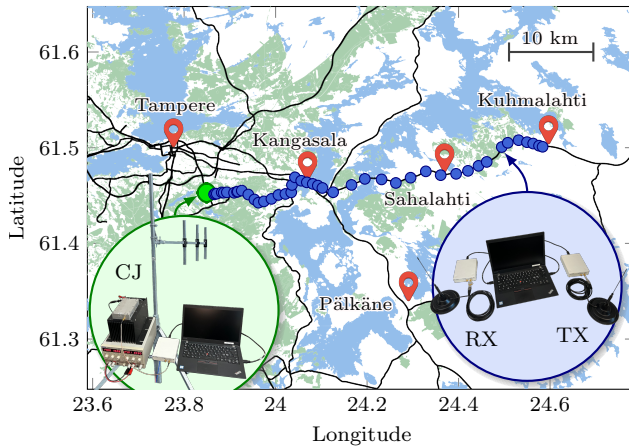
(b) Map view of the measurements

Fig. 8. Outdoor measurement setup.

Fig. 9. The received superposed KI and NBWF in the outdoor measurements at $1.3\,\mathrm{km}$ distance between the jammer and receiver.

Fig. 10. Outdoor KIC results depending on the distance between the jammer and receiver.

B. Measurement Results

The outdoor wireless propagation environment differs significantly from that in laboratory measurements, especially since the cabled connections therein essentially provided a single line-of-sight propagation path. It is the aim of this section to analyze the effect that these differences in propagation have on KIC. But first an example of the KI and NBWF waveforms recorded with the outdoor setup is given in the power spectral density plot of Fig. 9. It is visible that outdoors, unlike over cables as was shown in Fig. 4, the received KI signal is subject to noticeable frequency selectivity. This affects both the KI signal itself but also the nonlinear distortions that accompany the main signal. To compensate for this multipath propagation effect, KIC will need to model the outdoor propagation channel with more coefficients than what was necessary for the cabled channel.
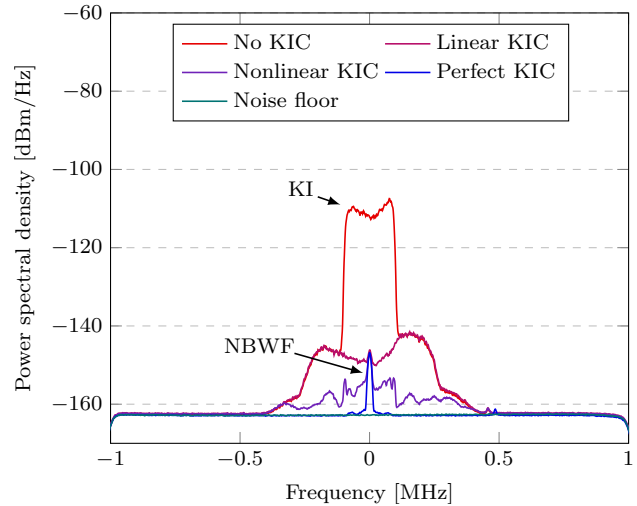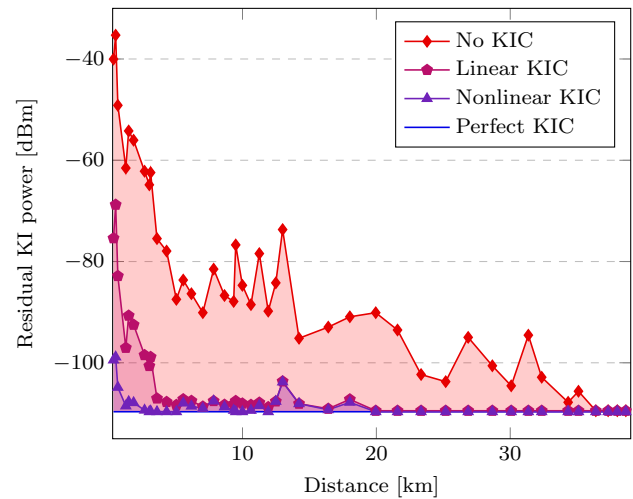
Outdoor measurement results without the NBWF and at different distances between the cooperative jammer and receiver are illustrated in Fig. 10. As expected, the received KI power decreases with the increase in the distance between the two devices, although the changes in the environment at different distances cause some variations in that trend. The processed measurement results show that both linear and nonlinear KIC variants are capable of suppressing the KI at the longer distances. However, the benefit of nonlinear KIC is highlighted by the measurement results at shorter distances, when the received nonlinear distortions are above the noise floor at the receiver. It can be observed that the nonlinear distortions in this outdoor measurement scenario reach the receiver with distances up to $4\,\mathrm{km}$. That is approximately 10% of the total coverage distance where the received KI is above the receiver noise floor. The same measurement data is plotted from a different point of view in Fig. 11 to give further insight into the KICs performance.
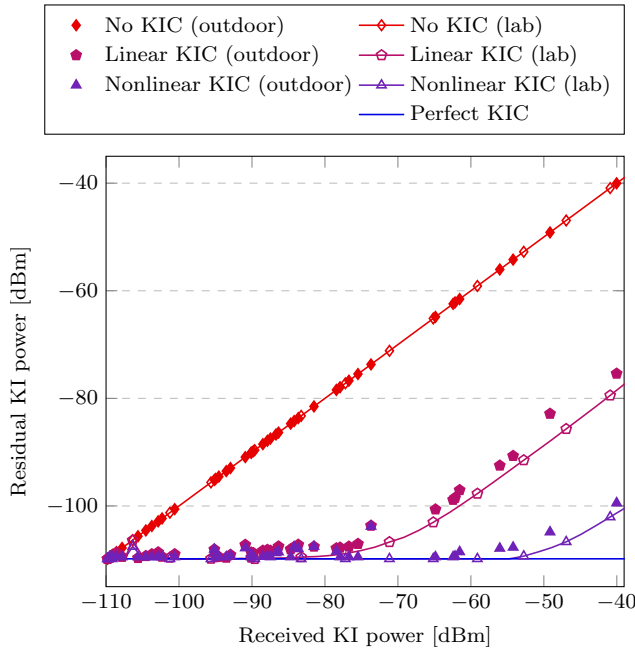
Fig. 11.   Outdoor and laboratory KIC results depending on the received KI power.
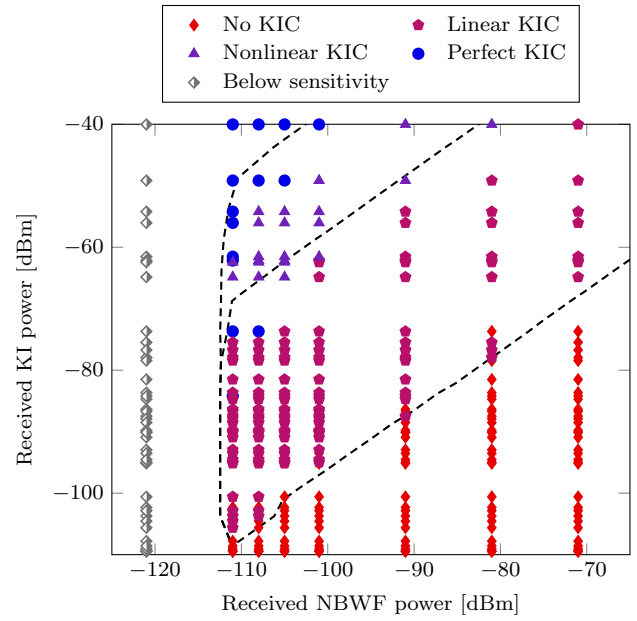

Fig. 12.   Outdoor and laboratory NBWF processing results, showing the minimum level of KIC required to achieve a BER lower than 10%.

In Fig. 11, the x-axis denotes the received KI power instead of the distance. This better visualizes performance of the KIC algorithms depending on the received KI power, but it also allows to compare the outdoor KIC results with the laboratory results from Section III. This comparison shows that in the outdoor environment, both KICs perform slightly worse than in the laboratory. This is likely because of the algorithms' inabilities to perfectly estimate all of the outdoor propagation paths as well as because of the rapid changes in these propagation paths that the algorithms cannot react to quickly enough. Still, both KIC algorithms manage to suppress the received KI considerably and incur only about a $3\,\mathrm{dB}$ performance penalty in the outdoor environment compared to the laboratory case. The outdoor cancellation results were achieved with convergence times similar to those of the laboratory measurements. That is, with convergence times up to $20\,\mathrm{ms}$ but typically below $5\,\mathrm{ms}$.

Finally, Fig. 12 illustrates the impact that KIC has on the NBWF processing. The different markers in Fig. 12 show what kind of processing capabilities (i.e., no KIC, linear KIC, nonlinear KIC, or perfect KIC) the receiver requires for the NBWF demodulation to reach a BER lower than 10% based on the outdoor measurements. The dashed lines in Fig. 12 show the same 10% BER thresholds but based on the laboratory measurement results from Section III. As was the case in comparing the two measurement sets in Fig. 11, it is again evident that the two KIC algorithms have a direct positive impact on the NBWF processing outdoors as they do over cables. However, the KIC algorithms perform slightly worse outdoors than in the laboratory. The NBWF processing performance loss outdoors is closely aligned with the $3\,\mathrm{dB}$ loss in KIC performance that was observed in Fig. 11.

V.   OPERATIONAL ANALYSIS

The preceding measurement results give a thorough understanding of how the two KIC algorithms perform given a specific SINR at the receiver in either ideal or practical conditions. However, besides understanding the capabilities of the developed algorithm in terms of the received signal levels, it is also interesting how these technical results convert to actual benefits on the battlefield. In this section, results from both laboratory and outdoor measurements are taken into account to study the impact that cooperative jamming and its suppression using KIC can achieve over a geographical area.

A.   Configuration

We simulated the impact of cooperative jamming and its cancellation over the same area where the outdoor measurements were carried out. The simulation results provide a functional tactical communication area, in which the BER at the tactical radio receiver is below the aforementioned 10^{-4} threshold. The simulations assumed that the transmitter and cooperative jammer were placed as illustrated in Fig. 13 and the communications performance was simulated depending on the receiver position and its KIC capabilities. The transmitter was assumed to have an output power of $5\,\mathrm{W}$ and structural antenna height of $2\,\mathrm{m}$ while the cooperative jammer was assumed to have an output power of $100\,\mathrm{W}$ and antenna at structural height of $30\,\mathrm{m}$. The receiver was assumed to have structural antenna height of $2\,\mathrm{m}$. These parameters, along with digital terrain elevation data [34], were then used in the irregular terrain model (ITM) [35], [36] to simulate the received KI and NBWF power levels, P_{KI} and P_{NBWF}, at the tactical radio receiver.
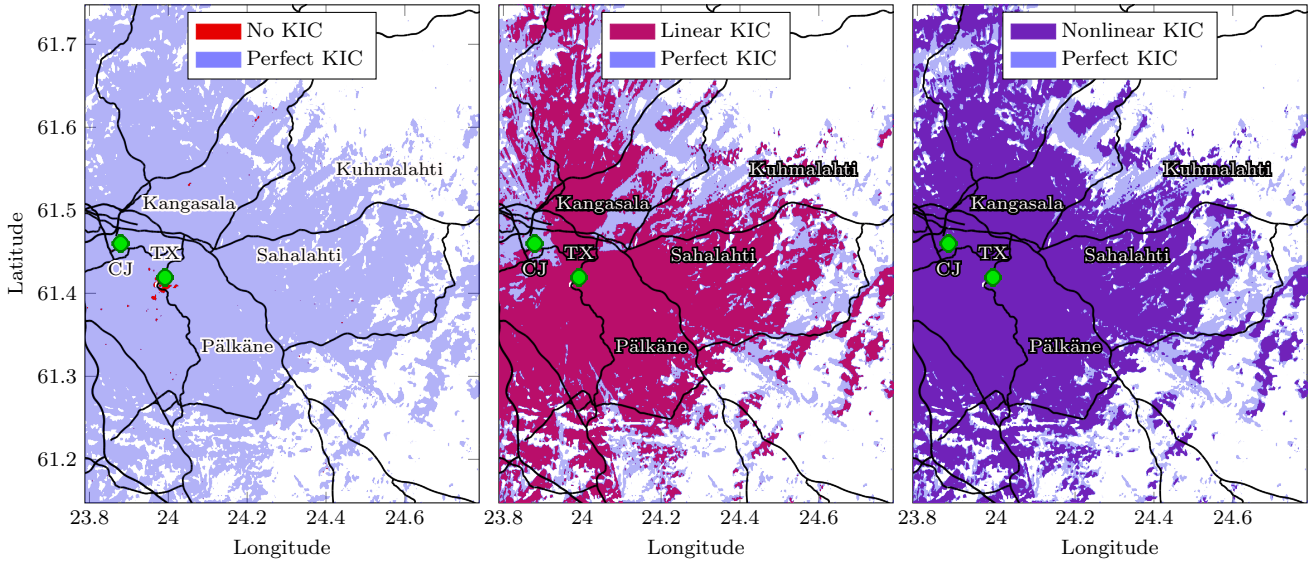
Fig. 13. Modeled functional tactical communication area (BER $\leq 10^{-4}$) under high-power cooperative jamming depending on the receiver capabilities (i.e., without or with KIC).

The simulated received KI and NBWF power levels were used together with the results presented so far to determine whether the receiver could successfully demodulate the received NBWF signal given its position and KIC capability. That is, the laboratory measurement results presented in Fig. 7 were first linearly interpolated to construct two-dimensional functions $\gamma_{\mathrm{W}}(P_{\mathrm{KI}}, P_{\mathrm{NBWF}})$, $\gamma_{\mathrm{L}}(P_{\mathrm{KI}}, P_{\mathrm{NBWF}})$, and $\gamma_{\mathrm{N}}(P_{\mathrm{KI}}, P_{\mathrm{NBWF}})$ that provide the SINR at the receiver without KIC, after linear KIC, or after nonlinear KIC, respectively. For the case with perfect KIC, the SINR was calculated by setting the received KI power to $0\,\mathrm{W}$ (i.e., using $\gamma_{\mathrm{W}}(-\infty, P_{\mathrm{NBWF}})$). It was then taken into account, based on the laboratory measurement results presented in Fig. 7, that to reach 10^{-4} BER, post-KIC SINR of at least $0\,\mathrm{dB}$ is required. And, based on the outdoor measurement results in Fig. 12, it was assessed that in practical conditions the post-KIC SINR is shifted by $3\,\mathrm{dB}$ in terms of the received KI power, which is equivalent to offsetting the received KI power for the linear and nonlinear KIC by $3\,\mathrm{dB}$.

For any given receiver position, the tactical communication link was then assessed to be functional based on

$$A_{\mathrm{W}} = \begin{cases} \text{True}, & \text{if } \gamma_{\mathrm{W}}(P_{\mathrm{KI}}, P_{\mathrm{NBWF}}) > 0 \\ \text{False}, & \text{otherwise} \end{cases} \quad (11)$$

$$A_{\mathrm{L}} = \begin{cases} \text{True}, & \text{if } \gamma_{\mathrm{L}}(P_{\mathrm{KI}} + 3, P_{\mathrm{NBWF}}) > 0 \\ \text{False}, & \text{otherwise} \end{cases} \quad (12)$$

$$A_{\mathrm{N}} = \begin{cases} \text{True}, & \text{if } \gamma_{\mathrm{N}}(P_{\mathrm{KI}} + 3, P_{\mathrm{NBWF}}) > 0 \\ \text{False}, & \text{otherwise} \end{cases} \quad (13)$$

$$A_{\mathrm{P}} = \begin{cases} \text{True}, & \text{if } \gamma_{\mathrm{W}}(-\infty, P_{\mathrm{NBWF}}) > 0 \\ \text{False}, & \text{otherwise} \end{cases} \quad (14)$$

for the cases without, with linear, with nonlinear, and with perfect KIC, respectively.

B. Results

Fig. 13 shows the simulated coverage results depending on the receiver capabilities. If the receiver has perfect KIC, then the communication distance between the transmitter and receiver is about $35\,\mathrm{km}$ (illustrated by the light blue area in all three plots of Fig. 13), the same communication distance that the two nodes could achieve if there was no jamming. Conversely, if the receiver has no KIC, then the communication distance is reduced to less than few kilometers by the cooperative jammer (illustrated by the red scattered area around the transmitter on the left-most plot in Fig. 13). However, given either KIC capability, the achievable communication distance increases drastically compared to that without KIC. Of course, neither KIC method facilitates the same communications distance that perfect KIC would, but in terms of functional communication area, the two methods come quite close.

The difference for the two KICs is not in the maximum communication distance but in the communication performance close to the cooperative jammer. With linear KIC (illustrated by the pink area in the middle plot of Fig. 13), the receiver has limited connectivity when positioned close to the cooperative jammer. With nonlinear KIC (illustrated by the purple area in the right-most plot of Fig. 13), communication is facilitated also when the receiver is adjacent to the cooperative jammer. The results in Fig. 13 illustrate the differences in areas that the enemy and host forces could expect to have functioning communications, given the fixed cooperative jammer and transmitter positions, transmit powers, and the specific terrain. However, the results also indicate how cooperative jamming with its suppression at the host receivers could, at the cost of a limited performance penalty to the host forces, help prevent an adversary from eavesdropping, detecting host force presence, and locating the host forces.

VI. CONCLUSION

In this work, a nonlinear known-interference cancellation (KIC) algorithm was proposed for suppressing the known interference (KI) received from a high-power cooperative jammer. The proposed algorithm estimates and tracks the nonlinear distortions, wireless propagation paths, carrier frequency offset, and sampling frequency offset affecting the received signal, given that the original transmitted signal is known to the receiver. By estimating these effects, the original KI can be matched to the received KI, and the received KI can be canceled from the total received signal. Cancellation of the received KI uncovers any other signals simultaneously received on the same frequency for further processing.

Measurements were carried out in controlled laboratory and practical outdoor environments, testing the algorithm in a range of signal-to-interference-plus-noise ratios (SINRs) and conditions. The outdoor measurements were carried out on land but there is no inherent limitation that would prevent the same technology from being used in other environments, such as in air or on water. Analysis of the results demonstrated that high-power cooperative jamming in combination with the proposed KIC method can be used to control access to the electromagnetic spectrum (EMS) with only a moderate performance penalty to the authorized nodes' sensitivity. Considering the significance of EMS on the modern battlefield as a cross-domain resource, this capability has the potential to positively impact outcomes in all of the warfighting domains.

APPENDIX A

This work relies on spline-based interpolation for modeling the nonlinear behavior of a PA, the basics of which are presented here. We assume a real-valued positive input signal $A(n)$ with maximum amplitude of $A_{\max}$ and a uniform spline interpolation scheme with knots spaced by Δ_A. In this work, $A(n)$ is taken to be the instantaneous magnitude of the resampled complex-valued signal $y(n)$. In a uniform spline interpolation scheme of P-th order, the input signal range is divided into $K = A_{\max}/\Delta_A$ regions that are accessed using the span index, abscissa value, and abscissa vector, defined respectively as

$$i_n = \left\lfloor \frac{A(n)}{\Delta_A} + 1 \right\rfloor, \tag{15}$$

$$u_n = \frac{A(n)}{\Delta_A} - (i_n - 1), \tag{16}$$

$$\mathbf{u}_n = \begin{bmatrix} u_n^P & u_n^{P-1} & \cdots & 1 \end{bmatrix}^T. \tag{17}$$

The spline-interpolated output corresponding to input $A(n)$ can then be written as

$$B(n) = \mathbf{\Psi}_n^T \mathbf{q}_n, \tag{18}$$

where $\mathbf{q}_n \in \mathbb{C}^{Q \times 1} = [q_0 \ q_1 \ \cdots \ q_{Q-1}]^T$ is the vector of spline control points with $Q = K + P$ elements and

$$\mathbf{\Psi}_n = \begin{bmatrix} 0 & \cdots & 0 & \mathbf{u}_n^T \mathbf{C} & 0 & \cdots & 0 \end{bmatrix}^T \tag{19}$$

is the spline basis function with the vector $\mathbf{u}_n^T \mathbf{C}$ positioned such that the starting index is i_n, in order to multiply the corresponding control points in $\mathbf{q}_n$, and $\mathbf{C}$ is a pre-computed matrix that contains the coefficients of the P-th order spline basis functions. In this work, 3rd order B-spline interpolation is used in which case the coefficients in $\mathbf{C}$ are [37]

$$\mathbf{C} = \frac{1}{6} \begin{bmatrix} \frac{-1}{\Delta_A^3} & \frac{3}{\Delta_A^3} & \frac{-3}{\Delta_A^3} & \frac{1}{\Delta_A^3} \\ \frac{3}{\Delta_A^2} & \frac{-6}{\Delta_A^2} & \frac{3}{\Delta_A^2} & 0 \\ \frac{-3}{\Delta_A} & 0 & \frac{3}{\Delta_A} & 0 \\ 1 & 4 & 1 & 0 \end{bmatrix}. \tag{20}$$

APPENDIX B

Deriving the update equations of an adaptive algorithm to minimize a cost function based on the gradient descent approach relies on one-by-one taking the partial derivatives of the cost function with respect to all of the adaptive algorithm's parameters, or parameter vectors, while assuming that the other parameters are constant. This results in a gradient vector that indicates how changes in the parameters affect the cost function and, therefore, facilitates updating the parameters so as to minimize the cost function. Gradient vector of the cost function in (6) is

$$\nabla J(n) = \left[\frac{\partial J(n)}{\partial \mathbf{h}_n^H}, \frac{\partial J(n)}{\partial \mathbf{q}_n^H}, \frac{\partial J(n)}{\partial \epsilon(n)}, \frac{\partial J(n)}{\partial \eta(n)} \right], \tag{21}$$

where the separate partial derivatives are expanded one-by-one in the following.

Taking the partial derivative of the cost function in (6) with respect to the filter coefficients $\mathbf{h}_n$ is similar to that of classical adaptive filters [38, p. 788] while the remaining parameters can be considered constant. This results in

$$\frac{\partial J(n)}{\partial \mathbf{h}_n^H} = \frac{\partial e(n)e^*(n)}{\partial \mathbf{h}_n^H} \tag{22}$$

$$= e^*(n)\frac{\partial e(n)}{\partial \mathbf{h}_n^H} + e(n)\frac{\partial e^*(n)}{\partial \mathbf{h}_n^H} \tag{23}$$

$$= -e^*(n)\frac{\partial \mathbf{h}_n^H \mathbf{r}_n e^{j\phi(n)}}{\partial \mathbf{h}_n^H} - 0 \tag{24}$$

$$= -e^*(n)\mathbf{r}_n e^{j\phi(n)}, \tag{25}$$

from what follows that the S-FO-LMS update equation for the filter coefficients is

$$\mathbf{h}_{n+1} = \mathbf{h}_n + \mu_{\mathrm{h}} e^*(n)\mathbf{r}_n e^{j\phi(n)}. \tag{26}$$

Similarly, partial derivative of the cost function with respect to the spline control points $\mathbf{q}_n$ yields

$$\frac{\partial J(n)}{\partial \mathbf{q}_n^H} = 0 - e(n)\frac{\partial \mathbf{r}_n^H \mathbf{h}_n}{\partial \mathbf{q}_n^H} e^{-j\phi(n)} \tag{27}$$

$$= -e(n)\frac{\partial \mathbf{r}_n^H}{\partial \mathbf{q}_n^H} \mathbf{h}_n e^{-j\phi(n)} \tag{28}$$

$$= -e(n)\mathbf{\Sigma}_n^T \mathbf{Y}_n^* \mathbf{h}_n e^{-j\phi(n)}, \tag{29}$$

where, assuming slowly changing $\mathbf{q}_n$,

$$\frac{\partial \mathbf{r}_n^H}{\partial \mathbf{q}_n^H} = \frac{\partial}{\partial \mathbf{q}_n^H}[r^*(n) \; \cdots \; r^*(n-M+1)] \tag{30}$$

$$= [y^*(n)\mathbf{\Psi}_n^* \; \cdots \; y^*(n-M+1)\mathbf{\Psi}_{n-M+1}^*] \tag{31}$$

$$= \mathbf{\Sigma}_n^T \mathbf{Y}_n^*. \tag{32}$$

As a result, the update equation for the spline control points is

$$\mathbf{q}_{n+1} = \mathbf{q}_n + \mu_{\mathrm{q}} e(n)\mathbf{\Sigma}_n^T \mathbf{Y}_n^* \mathbf{h}_n e^{-j\phi(n)}. \tag{33}$$

Taking the partial derivatives of the cost function with respect to the carrier and sampling frequency offsets gives

$$\frac{\partial J(n)}{\partial \epsilon(n)} \approx -e^*(n)\frac{\partial \mathbf{h}_n^H \mathbf{r}_n e^{j\phi(n)}}{\partial \epsilon(n)} \tag{34}$$

$$\approx -e^*(n)\mathbf{h}_n^H \mathbf{r}_n j e^{j\phi(n)} \tag{35}$$

and

$$\frac{\partial J(n)}{\partial \eta(n)} \approx -e^*(n)\frac{\partial \mathbf{h}_n^H \mathbf{r}_n e^{j\phi(n)}}{\partial \eta(n)} \tag{36}$$

$$\approx -e^*(n)\mathbf{h}_n^H \mathbf{r}_n' e^{j\phi(n)}, \tag{37}$$

respectively, where $(\cdot)'$ denotes a time derivative. The respective carrier and sampling frequency offset update equations in S-FO-LMS become

$$\epsilon(n+1) = \epsilon(n) - \mu_{\epsilon}\Im\{e^*(n)\mathbf{h}_n^H \mathbf{r}_n e^{j\phi(n)}\} \tag{38}$$

and

$$\eta(n+1) = \eta(n) + \mu_{\eta}\Re\{e^*(n)(\mathbf{h}_n^H \mathbf{r}_n)' e^{j\phi(n)}\}, \tag{39}$$

where the time derivative can be approximated using centered or backward first-order divided difference [24] based on $\mathbf{h}_n^H \mathbf{r}_n$ and $\mathbf{h}_{n-1}^H \mathbf{r}_{n-1}$ since these will have been calculated at iteration n anyway.

REFERENCES

[1] A. E. Spezio, "Electronic warfare systems," *IEEE Trans. Microw. Theory Techn.*, vol. 50, no. 3, pp. 633–644, Mar. 2002.

[2] L. Neng-Jing and Z. Yi-Ting, "A survey of radar ECM and ECCM," *IEEE Trans. Aerosp. Electron. Syst.*, vol. 31, no. 3, pp. 1110–1120, Jul. 1995.

[3] G. C. Tavik, C. L. Hilterbrick, J. B. Evins, J. J. Alter, J. G. Crnkovich, J. W. de Graaf, W. Habicht, G. P. Hrin *et al.*, "The advanced multifunction RF concept," *IEEE Trans. Microw. Theory Techn.*, vol. 53, no. 3, pp. 1009–1020, Mar. 2005.

[4] J. M. Hamamreh, H. M. Furqan, and H. Arslan, "Classifications and applications of physical layer security techniques for confidentiality: A comprehensive survey," *IEEE Commun. Surveys Tuts.*, vol. 21, no. 2, pp. 1773–1828, Oct. 2018.

[5] K. E. Kolodziej, B. T. Perry, and J. S. Herd, "In-band full-duplex technology: Techniques and systems survey," *IEEE Trans. Microw. Theory Techn.*, vol. 67, no. 7, pp. 3025–3041, Jul. 2019.

[6] G. Zheng, I. Krikidis, J. Li, A. P. Petropulu, and B. Ottersten, "Improving physical layer secrecy using full-duplex jamming receivers," *IEEE Trans. Signal Process.*, vol. 61, no. 20, pp. 4962–4974, Oct. 2013.

[7] G. Eriksson and E. Axell, "Physical limits for in-band full duplex in frequency-hopping tactical radio systems," in *Proc. Int. Conf. on Mil. Commun. and Inf. Syst.*, May 2023.

[8] K. Pärlin, T. Riihonen, V. Le Nir, M. Bowyer, T. Ranstrom, E. Axell, B. Asp, R. Ulman, M. Tschauner, and M. Adrat, "Full-duplex tactical information and electronic warfare systems," *IEEE Commun. Mag.*, vol. 59, no. 8, pp. 73–79, Aug. 2021.

[9] W. Guo, H. Zhao, W. Ma, C. Li, Z. Lu, and Y. Tang, "Effect of frequency offset on cooperative jamming cancellation in physical layer security," in *Proc. IEEE Globecom Workshops*, Dec. 2018.

[10] W. Guo, C. Li, H. Zhao, R. Wen, and Y. Tang, "Comprehensive effects of imperfect synchronization and channel estimation on known interference cancellation," *IEEE Trans. Veh. Technol.*, vol. 69, no. 1, pp. 457–470, Oct. 2019.

[11] C. Li, W. Guo, L. Zhang, X. Quan, Q. Xu, Y. Liu, and Y. Tang, "Impact of frequency offset on nonlinear distortion suppression in cooperative jamming communications," in *Proc. Int. Conf. on Commun. Workshops*, May 2019.

[12] W. Guo, C. Song, X. Xia, F. Hu, H. Zhao, S. Shao, and Y. Tang, "Analysis of cooperative jamming cancellation with imperfect time synchronization in physical layer security," *IEEE Wireless Commun. Lett.*, vol. 10, no. 2, pp. 335–338, Feb. 2021.

[13] C. Song, M. Zhao, W. Guo, C. Shi, H. Zhao, and S. Shao, "Artificial noise shielded frequency-hopping systems: Transceiver design and performance analysis," *IEEE Wireless Commun. Lett.*, vol. 10, no. 6, pp. 1286–1289, Jun. 2021.

[14] W. Guo, Y. He, H. Zhao, and S. Shao, "Impact of phase noise on nonlinear cooperative jamming cancellation in physical layer security," in *Proc. IEEE Int. Conf. on Commun.*, May 2022, pp. 3317–3321.

[15] C. Song, H. Zhao, L. Qin, R. Wen, and S. Shao, "Analysis and optimization of transceiver IQ imbalances in artificial noise shielded FH communication," *IEEE Trans. Signal Process.*, vol. 70, pp. 2798–2813, May 2022.

[16] W. Guo, H. Hu, Y. He, M. Yan, H. Zhao, and S. Shao, "Impacts of clock jitter on cooperative jamming cancellation," in *Proc. IEEE Global Commun. Conf.*, Dec. 2022, pp. 4142–4147.

[17] W. Guo, H. Zhao, and Y. Tang, "Testbed for cooperative jamming cancellation in physical layer security," *IEEE Wireless Commun. Lett.*, vol. 9, no. 2, pp. 240–243, Feb. 2020.

[18] W. Guo, M. Jin, Y. Fang, Y. He, H. Zhao, and S. Shao, "Time-frequency robust cooperative jamming cancellation for physical security in tactical networks," in *Proc. Int. Conf. on Commun. Workshops*, May 2023, pp. 1818–1823.

[19] J. M. Doty, R. W. Jackson, and D. L. Goeckel, "Analog cancellation of a known remote interference: Hardware realization and analysis," *IEEE Wireless Commun. Lett.*, no. 3, Mar. 2024.

[20] C. Li, W. Guo, X. Quan, Q. Xu, Y. Liu, Y. Shen, H. Zhao, and Y. Tang, "Nonlinear distortion suppression of cooperative jamming system for secure wireless communication," in *Proc. MTT-S Int. Microw. Symp.*, Jun. 2019, pp. 952–955.

[21] C. Li, Y. Liu, Q. Xu, and Y. Tang, "Self-interference cancellation with frequency offset and nonlinear distortion suppression for cooperative jamming communications," *IEEE Commun. Lett.*, vol. 23, no. 11, pp. 2091–2094, Nov. 2019.

[22] C. Li, X. Xia, C. Shi, L. Du, J. Ma, Y. Liu, and Y. Tang, "Cooperative jamming cancellation under nonlinearity and imperfect time-frequency alignments for physical-layer security," in *Proc. Int. Conf. on Commun. Workshops*, Jun. 2021.

[23] P. P. Campo, D. Korpi, L. Anttila, and M. Valkama, "Nonlinear digital cancellation in full-duplex devices using spline-based Hammerstein model," in *Proc. IEEE Globecom Workshops*, Dec. 2018.

[24] K. Pärlin, T. Riihonen, V. Le Nir, and M. Adrat, "Estimating and tracking wireless channels under carrier and sampling frequency offsets," *IEEE Trans. Signal Process.*, vol. 71, pp. 1053–1066, Mar. 2023.

[25] K. Pärlin, T. Riihonen, M. Turunen, V. Le Nir, and M. Adrat, "Known-interference cancellation in cooperative jamming: Experimental evaluation and benchmark algorithm performance," *IEEE Wireless Commun. Lett.*, vol. 12, pp. 1598–1602, Sep. 2023.

[26] ——, "Distributed cooperative jamming with multi-reference known-interference cancellation," in *Proc. Int. Conf. on Mil. Commun. and Inf. Syst.*, Apr. 2024.

[27] K. Pärlin, V. Le Nir, T. Meriläinen, A. Byman, M. Adrat, and T. Riihonen, "Wideband cooperative jamming with band-limited

known-interference cancellation," in *Proc. IEEE Mil. Commun. Conf.*, Oct. 2024.

[28] V. Lampu, L. Anttila, M. Turunen, and M. Valkama, "Gradient-adaptive 2-D LUT method for 6G flexible-duplex," *IEEE Microw. and Wireless Tech. Lett.*, 2024.

[29] L. Anttila, V. Lampu, S. A. Hassani, P. P. Campo, D. Korpi, M. Turunen, S. Pollin, and M. Valkama, "Full-duplexing with SDR devices: Algorithms, FPGA implementation, and real-time results," *IEEE Trans. Wireless Commun.*, vol. 20, no. 4, pp. 2205–2220, Apr. 2020.

[30] T. I. Laakso, "Splitting the unit delay," *IEEE Signal Process. Mag.*, vol. 13, no. 1, pp. 30–60, Jan. 1996.

[31] *Narrowband waveform for VHF/UHF radios*, North Atlantic Treaty Organization (NATO) Std. 5630, 2017, sTANAG 5630, Edition 1.

[32] V. Le Nir and B. Scheers, "Low complexity generic receiver for the NATO Narrow Band Waveform," in *Proc. Int. Conf. on Mil. Commun. and Inf. Syst.*, May 2017.

[33] M. Heino, E. Pöyry, M. Turunen, and T. Riihonen, "Design of high-isolation Yagi–Uda antennas for military full-duplex radios at 300 MHz," in *Proc. Int. Conf. on Mil. Commun. and Inf. Syst.*, May 2023.

[34] Copernicus Land Monitoring Service, "European Digital Elevation Model (EU-DEM), version 1.1," *https://ec.europa.eu/eurostat/web/gisco/geodata/digital-elevation-model/eu-dem*, 2016.

[35] G. A. Hufford, "The ITS Irregular Terrain Model, version 1.2.2: The algorithm," Institute for Telecommunication Sciences, Tech. Rep., 1999.

[36] National Telecommunications and Information Administration, "ITS Irregular Terrain Model," https://github.com/NTIA/itm, 2024.

[37] M. Scarpiniti, D. Comminiello, R. Parisi, and A. Uncini, "Non-linear spline adaptive filtering," *Signal Processing*, vol. 93, no. 4, pp. 772–783, Apr. 2013.

[38] S. Haykin, *Adaptive filter theory*, 5th ed. Pearson Education, 2014.

Karel Pärlin received his D.Sc. degree in communication engineering from Tampere University, Finland, in 2023, where he is currently continuing as a postdoctoral researcher. His research interests include adaptive signal processing, signal processing for communications, and physical layer security.

Matias Turunen is a researcher and a laboratory specialist at the Department of Electrical Engineering, Tampere University, Finland. His current research interests include digital pre-distortion methods, in-band full-duplex radios with an emphasis on analog RF cancellation, OFDM radar, and 5G new radio systems.

Aaron Byman [M'04] received the B.S.E.E. degree from the University of Washington, Seattle, WA, USA, in 1999 and the M.S.E.E. degree from the University of Oulu, Finland, in 2001. He is currently a senior specialist at Bittium, working in tactical communications and contributing mainly to the radio access layer. His areas of expertise include MIMO and OFDM(A) communications, synchroniza-tion, MIMO channel estimation and detection, and wideband code-division multiple-access technologies.

Tommi Meriläinen received the M.S.E.E degree from the University of Oulu, Finland in 2003. He is currently a principal RF engineer at Bittium, working in tactical communications and contributing mainly to the analog RF. His areas of expertise include RF architecture design, implementation and RF cancellation feasibility analysis.

Vincent Le Nir received his Ph.D. degree in electronics from the National Institute of Applied Sciences, France, in 2004. He is currently a senior researcher at the Royal Military Academy in Brussels, Belgium. His research interests are related to digital communications and signal processing in the wireless and wireline domains, MIMO communications, space–time coding, OFDM and multicarrier-code-division multiple-access, turbo-equalization, software defined and cognitive radio.

Marc Adrat received his Diploma and Dr.-Ing. degrees in electrical engineering from RWTH Aachen University, Germany, in 1997 and 2003, respectively. He is currently the head of the Software Defined Radio (SDR) research group at Fraunhofer FKIE in Wachtberg, Germany and an honorary professor at RWTH Aachen University, Germany. His research interests include digital signal processing for mobile tactical radio communications as well as emerging technologies like in-band full-duplex communications.

Taneli Riihonen [S'06, M'14, SM'22] received his D.Sc. degree in electrical engineering from Aalto University, Finland, in 2014. He is currently a tenure-track Associate Professor with the Faculty of Information Technology and Communication Sciences, Tampere University, Finland. His research interests include physical-layer OFDM(A), multiantenna, multi-hop, and full-duplex wireless techniques with current research interest includes the evolution of beyond 5G systems.